Magnetoelectric responses from the respective magnetic R and Fe subsystems in the noncentrosymmetric antiferromagnets $R\mathrm{Fe_3(BO_3)_4}$ (R = Eu, Gd, and Tb)

T. Kurumaji,[1] K. Ohgushi,[2] and Y. Tokura[1,3]

[1]*Department of Applied Physics and Quantum-Phase Electronics Center (QPEC), University of Tokyo, Tokyo 113-8656, Japan*

[2]*Institute for Solid State Physics, University of Tokyo, Kashiwanoha 5-1-5, Kashiwa, Chiba 277-8581, Japan*

[3]*RIKEN Center for Emergent Matter Science (CEMS), Wako 351-0198, Japan*

(Received 1 April 2014; published 20 May 2014)

In rare-earth (R) ferroborates, $R\mathrm{Fe_3(BO_3)_4}$ with R = Eu, Gd, and Tb, the magnetoelectric (ME) responses appear to stem from both the antiferromagnetic order of the iron (Fe) spins and the magnetic moments on the R ions. We measured the electric polarization (P) along the a axis while rotating a magnetic field (H) around the a axis and found that the target compounds show mutually distinctive H-direction dependencies. $\mathrm{EuFe_3(BO_3)_4}$ (R = Eu) shows an almost constant spontaneous P with a slight modulation when H is slanted from the c axis. The H-angle (θ_H) dependence of the P can be described by a formula $P = P_0 - \Lambda \sin^2\theta_H$. As for $\mathrm{GdFe_3(BO_3)_4}$ and $\mathrm{TbFe_3(BO_3)_4}$, they show highly anisotropic θ_H dependence of P, which characterizes the respective ME responses from their R magnetic moments. In certain regions of θ_H, the P can be described by $P = P_0 - K \sin 2\theta_H$ and $P = P_0 \mp \Gamma \sin\theta_H$ for R = Gd and Tb, respectively. We devised a theory for the ME response of the individual magnetic ions in a $R\mathrm{Fe_3(BO_3)_4}$ crystal and applied it to these compounds focusing on their local symmetry and their ground-state multiplet structures. The above formulas successfully reproduce the observed results as the summation of P from each magnetic subsystem, which in turn enables us to assign the first and second terms to the spontaneous P due to a collinear antiferromagnetic ordering of the Fe spins and the ME response of the R ion under H, respectively. The thermal and H-induced evolutions of the magnetic-ion resolved P quantitatively agree with the theoretical predictions, ensuring the relevant microscopic ME mechanism for each magnetic ion. The measurement of angular dependence of P is particularly useful to decompose the overlapped ME responses into the respective origins in the system with multiple magnetic subsystems.

DOI: 10.1103/PhysRevB.89.195126 PACS number(s): 75.85.+t, 76.30.Kg, 75.45.+j

I. INTRODUCTION

The physics of cross-correlated phenomena between magnetism and electricity in solids has a long history since the theoretical and experimental studies on the linear magnetoelectric (ME) effect [1–3]. Recent discoveries of multiferroicity in frustrated magnets including helimagnetic ferroelectric $\mathrm{TbMnO_3}$ [4] and the strong ME coupling in noncentrosymmetric magnets [5] have stimulated revived interest on the interrelation between ordered magnetic structure and dielectric property [6,7]. While there were extensive studies on the ME responses in solids, the understanding of the atomic mechanism of spin-induced electric polarization (P) has been limited in compounds with 3d transition metals. The behavior of the system with different kinds of magnetic ions coexisting such as 3d and 4f elements has remained elusive.

One of the examples of such materials is the family of rare-earth (R) ferroborates, $R\mathrm{Fe_3(BO_3)_4}$, which have received much attention because of the diverse ME responses with respect to R ions such as R = Y, Pr, Nd, Sm, Gd, and Tb [8–11]. The crystal structure of $R\mathrm{Fe_3(BO_3)_4}$ is shown in Fig. 1(a). Iron (Fe) ions are linked to form a helicoidal chain along the c axis [Fig. 1(b)]. R ions are located between three equivalent Fe chains [12,13]. Studies on specific heat [14], magnetization (M) [10,15,16], magnetic resonance [17,18], and neutron/x-ray scattering [19–22] have revealed that the Néel temperatures (T_N) are at 30 $\sim$ 40 K and their magnetic structure is basically of two-sublattice type with Fe spins ferromagnetically aligning in the ab plane and antiferromagnetically stacking along the c axis. The R ion with a magnetic moment critically influences the magnetic ground state, especially the direction of the Fe spins through the f-d coupling.

In many cases of $R\mathrm{Fe_3(BO_3)_4}$, the observation of a spontaneous P under a magnetic field (H) along the crystal axes ascertains the ME nature of these compounds. However, the P measurement alone provides only limited information on the microscopic origins of the H-induced P because the possibly two components of the ME responses from the different magnetic subsystems are superimposed. While there was a group theoretical approach to Fe-spin-induced P or discussion about possible linear ME effect on R site [8,23], the contribution from the other subsystem was ignored in the respective considerations. In this work, we show the effective methodology to solve such an issue, specifically decomposition of P into components for each magnetic subsystem. We measured P under rotating H in ferroborates with various R ions and observed the mutually different H-angle dependencies of P. We analyzed the ME responses of the individual magnetic ions focusing on their quantum mechanical features and found that the observed behaviors are reasonably described by the summation of P from each magnetic ion and that the magnetic anisotropy of the R ion discriminates the respective ME responses. The evolution of the magnetic-ion resolved P with temperature (T) and H quantitatively agree with the theoretical predictions, which ensures the relevant ME mechanism for each magnetic ion.

In this work, we focus on the three kinds of R ferroborates for R = Eu, Gd, and Tb. Their magnetic properties have been extensively investigated by various experimental methods and the P along the a axis under $H \parallel c$ or $H \perp c$ is observed

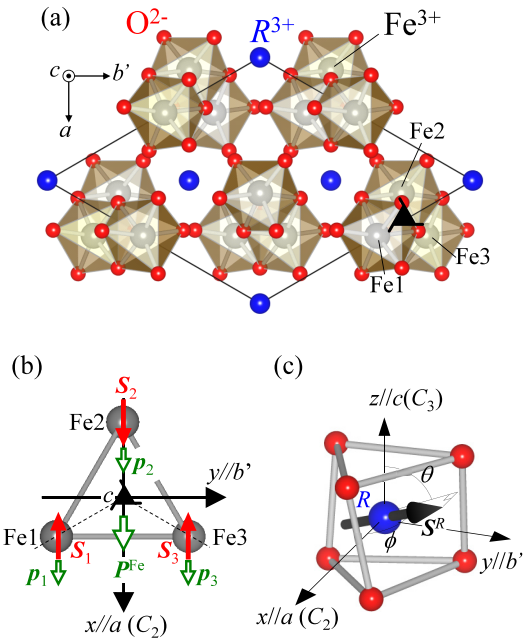

FIG. 1. (Color online) (a) Crystal structure of $R\mathrm{Fe}_3(\mathrm{BO}_3)_4$ belonging to the space group $R32$ (boron ions are not shown). The b' axis is defined for convenience, which intersects at right angles with the one of the a axes and the c axis. A windmill-like triangle indicates a threefold screw axis (3_1), which is one of the symmetry elements for an Fe helicoid (Fe1 $\sim$ Fe3). (b) The schematic illustration of the collinear antiferromagnetic structure on an Fe helicoid viewed from the c axis. Red arrows are the spins at the Fe sites ($\boldsymbol{S}_1 \sim \boldsymbol{S}_3$), and small green arrows indicate the local spin-induced electric dipole moments ($\boldsymbol{p}_1 \sim \boldsymbol{p}_3$). A large green arrow is the summation of them ($\boldsymbol{P}^{\mathrm{Fe}}$). The C_2 indicates the twofold rotation symmetry along the a axis at the Fe2 site. (c) A RO_6 polyhedron in the $R32$ structure. The C_2 and the C_3 are symmetry elements at the R site: a twofold and the threefold rotation axis, respectively. A large black arrow indicates the R magnetic moment ($\boldsymbol{S}^R$). The spherical coordinates ϕ and θ are defined as the polar and the azimuth angle, respectively.

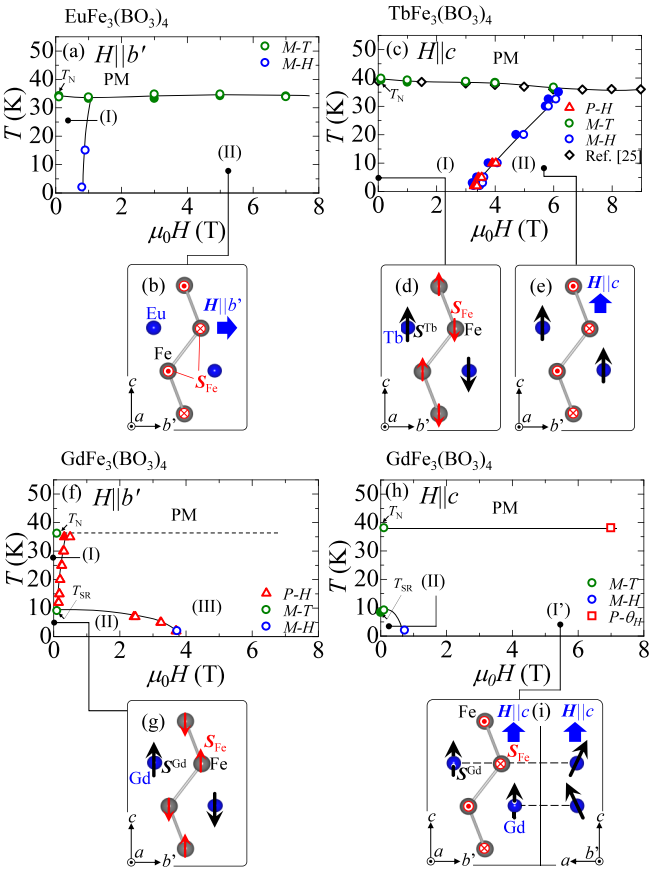

FIG. 2. (Color online) (a) The H-T phase diagram for $\mathrm{EuFe}_3(\mathrm{BO}_3)_4$ under $H \parallel b'$, determined by various T and H scans of M. Open (filled) characters are taken from the T- or the H-increasing (decreasing) scans. PM indicates the paramagnetic phase. (b) The schematic illustration of the magnetic structure of phase II. Red $\odot$ ($\otimes$) indicates that the Fe spin ($\boldsymbol{S}_{\mathrm{Fe}}$) is parallel (antiparallel) to the a axis. (c)–(i) Corresponding H-T phase diagrams for $\mathrm{GdFe}_3(\mathrm{BO}_3)_4$ and $\mathrm{TbFe}_3(\mathrm{BO}_3)_4$ under $H \parallel b'$ or $H \parallel c$ and the schematic illustrations of the magnetic structures. In (c), the black diamonds are taken from Ref. [25]. In (f), the dashed lines are the presumed phase boundary between the PM and the magnetic-ordered phase III. The right panel of (i) indicates the side view of the Gd sites with magnetic moments.

[8–10,24,25], which characterizes their magnetoelectricity. Figures 2(a)–2(h) reproduce the H-T phase diagrams and the schematic illustrations of the magnetic structures of the corresponding phases. We plot here the positions of anomalies of M and P measured at various H and T with our own samples, which are consistent with the previous reports [8–10,15,16,25].

$\mathrm{EuFe}_3(\mathrm{BO}_3)_4$ has an antiferromagnetic order below $T_{\mathrm{N}} = 34$ K [14,26]. The anisotropic magnetic susceptibilities suggest the easy-plane magnetic ordering of Fe spins [10]. While the magnetic structure in the low-H region (phase I) including the ground state has not been clarified, nonmonotonic M-H curves under $H \perp c$ suggest that the in-plane H reorients the Fe spins perpendicular to the H [Fig. 2(b)] to induce phase II.

$\mathrm{GdFe}_3(\mathrm{BO}_3)_4$ undergoes successive antiferromagnetic transitions at $T_{\mathrm{N}} = 37$ K and $T_{\mathrm{SR}} = 9$ K with $H = 0$ [Fig. 2(f)] [15,17,27]. In phase I, it is suggested that both Gd and Fe spins lie almost in the ab plane [8,17], yet a recent x-ray scattering study reported the incommensurability with a long wavelength ($\sim$370 nm) and the canting of the spins towards the c axis [19]. Below T_{SR}, the system goes to phase II [Fig. 2(f)], in which both Gd and Fe spins are reoriented along the c axis [Fig. 2(g)].

In phase II, either in-plane or out-of-plane H drives spin-flop transitions into phase III [Fig. 2(f)] and phase I′ [Fig. 2(h)], respectively [15]. It is suggested that in both phases the Fe spins flop to the ab basal plane with their moments perpendicular to H [8,17,18,28]. The magnetic structure of phase I′ is schematically illustrated in Fig. 2(i), which was theoretically suggested in Ref. [17] with a simple spin Hamiltonian for Gd and Fe ions. The Gd spins are noncollinear as illustrated in the right panel of Fig. 2(i) due to the balance between the Zeeman term and the in-plane f-d interaction, i.e., molecular field from the Fe subsystem. While the relationship between phases I and I′ is not clear because neither an incommensurability under $H \parallel c$ nor a phase boundary has been found as yet, we use the term "phase I′" only when a crystal is under H.

$TbFe_3(BO_3)_4$ shows the antiferromagnetic order below $T_N = 40$ K, in which magnetic moments of both Fe and Tb ions are parallel to the c axis [Fig. 2(d)] [16,20]. Metamagnetic-like transition into phase II under $H \parallel c$ [Fig. 2(c)] was also reported. In this phase, it is suggested that the Tb subsystem ferromagnetically polarizes along the c axis while the Fe subsystem is reoriented to the ab basal plane [Fig. 2(e)] [16,20,22].

The format of this paper is as follows: Section II shows theoretical studies on the ME couplings of an ordered Fe subsystem and that of a R-site magnetic moment. We treat their magnetic moments as operators to deduce the formulas of the spontaneous or the H-induced P as functions of T and H. Applications to the specific R ferroborates are also performed focusing on the features of the ground-state multiplets of their $4f$ electrons. The experimental details and the results are given in Secs. III and IV, respectively. Based on the preceding microscopic theories, the observed P are decomposed into components for respective magnetic subsystems and the identifications of their origins are discussed. The conclusion is given in Sec. V.

II. QUANTUM THEORY FOR MAGNETOELECTRIC RESPONSE IN RFe$_3$(BO$_3$)$_4$

Our basic idea is that the ME responses of these systems can be expressed by the summation of the P from respective magnetic subsystems. In this section, we theoretically consider the ME coupling for each magnetic ion. Specific formulas for the spin- or H-induced P are given as functions of T and H, which are used to reproduce the observed ME responses in the respective compounds.

Note that our target compounds show structural phase transitions at the temperature T_S ($T_S = 58$ K [26], 156 K [29], and 192 K [16] for R = Eu, Gd, and Tb, respectively) with a slight distortion of one of the three Fe helicoidal chains and symmetry lowering of R sites from D_3 into C_2, which is characterized by the changing of the space group from $R32$ to $P3_121$ [13,14,29]. In the present theory, we ignore the influence of the transition for simplicity and treat the crystal in the high symmetric space group $R32$; this will be justified because the crystal keeps the same point group D_3 through the structural transition, which appears not to change the macroscopic model parameters and hence not to alter the conclusion.

A. Electric polarization induced by Fe-spin ordering

First, we discuss the contribution of the Fe subsystem to the spontaneous P. The emergence of P on the background of the in-plane antiferromagnetic ordering of the Fe spins can be justified from the viewpoint of symmetry. The magnetic order of the Fe spins, for example, along one of the a axes eliminates the threefold rotational symmetry from the set of the D_3 symmetry elements. As a result, the crystal goes to a polar point group C_2, which allows the P along the a axis [Fig. 1(b)]. While the same conclusion was obtained with the Landau's free-energy expansion by the antiferromagnetic order parameter $\boldsymbol{L}$ of the Fe spins [8], there has been less discussion on the microscopic origin of the P. As for the candidates of the microscopic origin for spin-induced P on transition-metal ions, three different mechanisms are known: the exchange striction mechanism [30], the inverse Dzyaloshinskii-Moriya or spin-current mechanism [31,32], and the spin-dependent metal-ligand (d-p) hybridization mechanism [33]. The first two of them are involving the neighboring-spin correlation through a magnetic order such as a four-sublattice ($\uparrow\uparrow\downarrow\downarrow$) structure or a helimagnetic order, whereas the last one is originating from a spin moment at a single site. In the present case, the two-sublattice antiferromagnetic order with collinear spin alignment cannot induce the P by the first two of them. Thus, we only focus on the last one with taking account of its quantum mechanical nature, which gives a theoretical formula Eq. (8) for the Fe-induced P.

In the scenario of the d-p hybridization mechanism, the hybridization among a transition metal d orbital and a ligand p orbital is modulated by a d-spin through the spin-orbit interaction. The existence of the spin-dependent electric dipole moment $\boldsymbol{p}$ along the metal-ligand bond direction is predicted as

$$\boldsymbol{p} = t(\boldsymbol{e} \cdot \boldsymbol{S})^2 \boldsymbol{e}, \tag{1}$$

where $\boldsymbol{S}$ is a spin on the metal site, $\boldsymbol{e}$ a unit vector along the bond, and t a coupling constant related with the d-p hybridization and the spin-orbit interaction. Summation of $\boldsymbol{p}$ should be taken for all relevant bonds surrounding the metal ion site. Note that this summation remains finite only when the site symmetry of the metal ion belongs to the class of the piezoelectric point group. In the case of the present crystal, a unit cell contains three types of Fe sites (Fe1 $\sim$ Fe3), which are copies of each other in the threefold screw (3_1) symmetry along the c axis [Fig. 1(a)]. The Fe ion is surrounded by an O_6 octahedron and has a site symmetry of piezoelectric C_2. Thus, magnetic moments on the Fe sites are expected to induce local $\boldsymbol{p}$ through the d-p hybridization mechanism.

The actual functional form of the $\boldsymbol{p}_n$ for the Fe nth site (n = 1, 2, and 3) with respect to the $\boldsymbol{S}_n$ can be obtained by calculating Eq. (1) with the structural information of an FeO_6 octahedron. We skip this cumbersome process and instead introduce a modified form as follows:

$$p_{ni} = \sum_{j,k=x,y,z} \tau^n_{ijk} \langle \hat{S}_{nj} \hat{S}_{nk} \rangle - p'_{ni}. \tag{2}$$

We retained the quadratic form of the $\boldsymbol{S}_n$ as Eq. (1), but the structural detail is embedded in the tensor τ^n_{ijk}. Moreover, we treat the spin moment as an operator ($\hat{S}_n$). By taking the statistical average with a single-site spin Hamiltonian $\hat{\mathcal{H}}_n$ of the nth Fe ion as indicated by the brackets $\langle\ \rangle$, the T dependence of P can be deduced. The constant value p'_{ni} is needed because Eq. (2) should be zero in a paramagnetic state under $H = 0$. Let us now take $\hat{\mathcal{H}}_n = g\mu_B H_{mol} \hat{S}_{nx}$, that is, the spin Hamiltonian under a molecular field H_{mol} ($\propto \langle \hat{S}_{nx} \rangle$) for the antiferromagnetic order with the Fe spins along the a (x) axis [Fig. 1(b)]. We neglect the single-site anisotropy and the dipole-dipole interaction because they give anisotropy fields at most 10^3 Oe, which are negligibly small compared with the exchange field ($H_{mol} \sim 10^5$ Oe) [17,18]. We also omitted the f-d coupling with the R moment and Zeeman term, for simplicity of calculation. Actually, its magnitude is at most 70 000 Oe [28] in $GdFe_3(BO_3)_4$ and 38 000 Oe [26]

in $TbFe_3(BO_3)_4$, which is not so serious as the predominant Fe-Fe coupling.

Since the $\hat{\mathcal{H}}_n$ is cylindrically symmetric around the x axis, only the x component of the p_{ni} of the following form remains,

$$p_{nx} = \tau^n_{xxx}\langle \hat{S}^2_{nx}\rangle - p'_{nx}. \tag{3}$$

For a crystal of volume V containing $3N$ Fe ions, the macroscopic P derived from the Fe subsystem ($\boldsymbol{P}^{\mathrm{Fe}}$) is represented by $\boldsymbol{P}^{\mathrm{Fe}} = \frac{N}{V}(\boldsymbol{p}_1 + \boldsymbol{p}_2 + \boldsymbol{p}_3)$, being parallel to the x axis, and given as

$$P^{\mathrm{Fe}}_x = \frac{N}{V}\sum_{n=1,2,3}\left(\tau^n_{xxx}\langle \hat{S}^2_{nx}\rangle - p'_{nx}\right). \tag{4}$$

For the computation of the statistical average, we use the formula [34]

$$\langle \hat{S}^2_{nx}\rangle = S^2\left[B^2_S(u) + B'_S(u)\right], \tag{5}$$

where $B_S(u)$ is the Brillouin function for the spin quantum number $S = \frac{5}{2}$. The variable u is related with $T_{\mathrm{N}}(\propto H_{\mathrm{mol}})$ and is computable by solving the following equations self-consistently at each T [35]:

$$u = \frac{3T_{\mathrm{N}}\langle \hat{S}_x\rangle}{T(S+1)}, \tag{6}$$

$$\langle \hat{S}_{nx}\rangle = SB_S(u). \tag{7}$$

Substituting Eq. (5) into Eq. (4), the formula for the T dependence of the spontaneous P induced by the collinear antiferromagnetic order of the Fe subsystem is deduced as

$$P^{\mathrm{Fe}}_x = \tau\left(S^2\left[B^2_S(u) + B'_S(u)\right] - \frac{S+1}{3S}\right), \tag{8}$$

where $\tau \equiv \frac{N}{V}\sum_n \tau^n_{xxx}$. The factor $\frac{S+1}{3S}$ is necessary for the same reason for the introduction of p'_{ni}. Note that $\boldsymbol{P}^{\mathrm{Fe}} \parallel a$ is consistent with the above discussion on the symmetry of the magnetic structure. We will apply this formula for the interpretation of the following experimental results. Practically, T_{N} in u is set for each $RFe_3(BO_3)_4$ and only the unknown parameter τ will be adjusted so as to reproduce the experimental data.

B. ME coupling at the *R* site

The variation in the magnitude of the observed P among various $RFe_3(BO_3)_4$ indicates that the magnetic moment at the R site as well as the magnetic order of the Fe subsystem contributes to the ME response. While the possible ME properties of R ions were previously discussed in the studies of the conventional linear ME effect by Rado [36], the detailed understanding remains elusive. In this section, the general formula for the R-induced P and its applications to specific ions (R = Eu, Gd, and Tb) in $RFe_3(BO_3)_4$ under H are given.

The total angular momentum J ($= L + S$) becomes a good quantum number for the electronic structure of a $4f$ element within the LS coupling scheme. When the R ion is in a crystal, the electrostatic potential from the surrounding ions splits and shifts the degenerate $2J + 1$ levels and only a few of these levels often remain nearly degenerate as the ground-state multiplet. In such a case, we use pseudospin operators ($\hat{S}^R_x, \hat{S}^R_y$, and $\hat{S}^R_z$), which only act among the multiplet. Here, we assume that $\boldsymbol{p}$ at the R site can be described in the same manner of Eq. (2) by replacing $\hat{\boldsymbol{S}}_i$ with $\hat{\boldsymbol{S}}^R$ and/or $\boldsymbol{H}$. The P derived by the N R ions ($\boldsymbol{P}^R$) can be represented by

$$P^R_i = \frac{N}{V}\sum_{j,k=x,y,z}\left(\kappa_{ijk}\langle \hat{S}^R_j \hat{S}^R_k\rangle + \gamma_{ijk}\langle \hat{S}^R_j\rangle H_k + \lambda_{ijk}H_jH_k\right). \tag{9}$$

The first term corresponds to the spin-induced spontaneous P, which may originate from the similar d-p hybridization mechanism for transition-metal ions. The second and the third terms are related with the first- and second-order ME effects, respectively. The ME coupling tensors κ_{ijk}, γ_{ijk}, and λ_{ijk} are common for all the R ions in the crystal, but their magnitudes vary with the kind of R. Hereafter, we omit the scaling parameter $\frac{N}{V}$, which can be absorbed into the parameters κ_{ijk}, γ_{ijk}, and λ_{ijk}. The brackets $\langle\ \rangle$ indicate the statistical average of the operators taken by a single-site spin Hamiltonian of the R ion.

Mutual relationships among the nonzero components of the respective tensors κ_{ijk}, γ_{ijk}, and λ_{ijk} can be derived by the group theory [37]. For example, the symmetry of κ_{ijk} is the same as that of the piezoelectric tensor. Specifically, in a $RFe_3(BO_3)_4$ crystal with the $R32$ symmetry, the site symmetry of a R ion is piezoelectric D_3. In such a case, components of the tensors with $i = x$ are linked with each other by the relationships such as $\kappa_{xxx} = -\kappa_{xyy}$ ($\equiv\kappa'$), $\kappa_{xyz} = \kappa_{xzy}$ ($\equiv\frac{\kappa}{2}$), $\gamma_{xxx} = -\gamma_{xyy}$ ($\equiv\gamma'$), γ_{xyz} ($\equiv\gamma''$), γ_{xzy} ($\equiv\gamma$), $\lambda_{xxx} = -\lambda_{xyy}$ ($\equiv\lambda$), and $\lambda_{xyz} = \lambda_{xzy}$ ($\equiv\frac{\lambda'}{2}$), and otherwise zero. Here, we define a Cartesian coordinate for a RO_6 polyhedron as in Fig. 1(c). In the remaining part of this section, we will focus on each ground-state multiplet of a R ion for R = Eu, Gd, and Tb to deduce the specific forms of their P^R. Especially, P^R_x with H in an arbitrary direction will be given, which is applicable to the analysis of the following experimental results on the P along the a (x) axis under rotating H in the $b'c$ (yz) plane.

For $EuFe_3(BO_3)_4$, Eu ions contribute to P as

$$P^{\mathrm{Eu}}_x = \lambda\left(H^2_x - H^2_y\right) + \lambda' H_y H_z. \tag{10}$$

The terms proportional to κ_{ijk} and γ_{ijk} were removed since we do not need any pseudospin operator for the ground state $J = 0$ of Eu^{3+}. The remaining λ terms may be due to the H-induced moment, which corresponds to van Vleck paramagnetism through the excited multiplet $^7F_1$.

In the case of $GdFe_3(BO_3)_4$, a Gd^{3+} ion has a spin of $S = \frac{7}{2}$, which is described by a real-spin operator, $\hat{\boldsymbol{S}}^{\mathrm{Gd}}$. The specific formula of P^{Gd}_x is written as

$$P^{\mathrm{Gd}}_x = \kappa'\left\langle \hat{S}^2_x - \hat{S}^2_y\right\rangle + \kappa\langle \hat{S}_y\hat{S}_z\rangle + \gamma'(\langle \hat{S}_x\rangle H_x - \langle \hat{S}_y\rangle H_y) + \gamma''\langle \hat{S}_y\rangle H_z + \gamma\langle \hat{S}_z\rangle H_y. \tag{11}$$

Here, we omit the λ terms, which are assumed to be much smaller than the other two real-spin related terms. To take a statistical average we need a spin Hamiltonian of the Gd ion, which will be discussed in Sec. IV B.

The Ising nature of a Tb^{3+} ion in $TbFe_3(BO_3)_4$ is described by pseudospin operators with $S = \frac{1}{2}$, which are proportional to the Pauli matrices. Indeed, a recent spectroscopic study of this compound [38] revealed that its ground state is composed

of a non-Kramers doublet with the lowest excited state lying sufficiently high (by ~200 cm^{-1}) above them. The resultant formula is

$$P_x^{\mathrm{Tb}} = \gamma \langle \hat{S}_z \rangle H_y. \tag{12}$$

We omitted the terms $\kappa_{ijk}\hat{S}_j^{\mathrm{Tb}}\hat{S}_k^{\mathrm{Tb}}$ because they become constant, and also omitted the λ terms for the same reason in Eq. (11). As for the γ terms we only have to treat the above one, because a huge Ising anisotropy ($g_c \sim 18$, $g_a \sim 0$) [38] confines the Tb moment along the z (c) axis. Note that the pseudospin operator does not work as an axial vector because the Tb^{3+} ion is a non-Kramers ion. As Griffith [39] warned to use the pseudospin operators to describe the magnetic and spectroscopic properties of such system, we also need a special care in the discussion of ME responses. Fortunately, the validity of the form of Eq. (12) was previously proved in the context of the electric-field (E) effect in paramagnetic resonance within the ligand-field theory by Washimiya *et al.* [40].

With these specific forms of P^R, each $R\mathrm{Fe_3(BO_3)_4}$ is expected to show anisotropic P under rotating H. In the following section, we report on the mutually distinctive ME responses, which will be decomposed into origins for each magnetic subsystem with the help of the above formulas.

III. EXPERIMENTAL METHODS

Single crystals of $R\mathrm{Fe_3(BO_3)_4}$ (R = Eu, Gd, and Tb) were grown from flux of $[100-n]$ mass %$(\mathrm{Bi_2Mo_3O_{12}} + p\mathrm{B_2O_3} + q\mathrm{R_2O_3}) + n$ mass %$[R\mathrm{Fe_3(BO_3)_4}]$ composition with $n = 25$, $p = 3$, and $q = 0.6$ to grow $\mathrm{EuFe_3(BO_3)_4}$, with $n = 25$, $p = 2$, and $q = 0.6$ to grow $\mathrm{GdFe_3(BO_3)_4}$ [41], and with $n = 25$, $p = 2.5$, and $q = 0.5$ to grow $\mathrm{TbFe_3(BO_3)_4}$ [20]. In each case, the flux with a total mass of 60 g was prepared in a cylindrical platinum crucible by successive melting of $(\mathrm{Bi_2O_3}+\mathrm{MoO_3})$ at 600 °C and $(\mathrm{B_2O_3} + \mathrm{R_2O_3}+\mathrm{Fe_2O_3})$ at 1000 °C. The flux was kept at 1000 °C for several hours, and the flux temperature was gradually decreased to 860 °C. The prismatic green crystals with size of 2–5 mm were obtained.

The orientation of the crystals was determined by Laue x-ray diffractometry. The crystal surfaces were assigned to the combination of rhombohedra $\{10\bar{1}1\}$ and trigonal prisms $\{2\bar{1}\bar{1}0\}$ and $\{\bar{2}110\}$. Here, the sense of the rhombohedra is tentative just for the definition of the rotational direction of the H. For polarization measurements the crystals were polished with the end faces perpendicular to the a axis and silver paste was painted on the two parallel surfaces as the electrodes. P was deduced by the time integration of the polarization current measured with a constant rate of H rotation (2 °/sec) or H sweep (80 Oe/sec). The H was rotated around the $[2\bar{1}\bar{1}0]$ (a) axis. The rotational direction of the H is defined as clockwise when it is rotated from the [0001] (c) axis towards the $[01\bar{1}0]$ (b') axis. M was measured using a Quantum Design magnetic property measurement system (MPMS) and physical property measurement system (PPMS).

IV. RESULTS AND DISCUSSION

A. ME responses in $\mathrm{EuFe_3(BO_3)_4}$

We begin with the results on $\mathrm{EuFe_3(BO_3)_4}$. This is because its phase diagram [Fig. 2(a)] and the predicted ME response

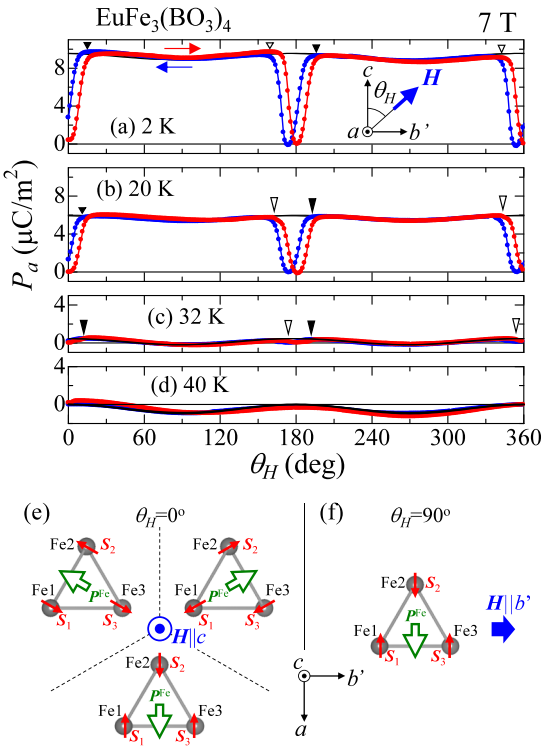

FIG. 3. (Color online) (a)–(d) P along the a axis measured at various T with $\mu_0 H = 7$ T as functions of the angle of the H (θ_H). The solid curves are fits with Eq. (13). (e) The schematic illustration of three equivalently stable magnetic domains under $H \parallel c$. Corresponding $\boldsymbol{P}^{\mathrm{Fe}}$ are indicated. (f) The unique collinear magnetic structure chosen under $H \parallel b'$.

of a Eu ion [Eq. (10)] are simple compared with those of the other two compounds with the rare-earth moment. The P along the a axis was measured in rotating H around the a axis for $\mathrm{EuFe_3(BO_3)_4}$. Figures 3(a)–3(d) show P_a as functions of the H angle (θ_H), measured at 7 T and at various T. The θ_H is defined as the angle from the c axis to the H when the H is rotated in a clockwise manner. Note that the magnitude of H is sufficient to induce the ME phase II under $H \parallel b'$ [Fig. 2(a)].

At 2 K and 20 K [Figs. 3(a) and 3(b)], the emergence of P is observed as H is inclined from the c axis ($\theta_H = 0°, 180°$) towards the b' axis, which are indicated by closed and open triangles (▼ and ▽); this is interpreted as follows. The collinear magnetic order of the Fe subsystem has three possible magnetic domains with spontaneous P ($\boldsymbol{P}^{\mathrm{Fe}}$) along one of the a axes [Fig. 3(e)]. Since they are equivalently stable under $H \parallel c$ ($\theta_H = 0, 180°$), each domain is equally populated to cancel P ($P_a = 0$). As the H is inclined towards the b' axis, one of the three domains is selected to form a single domain, which allows the emergence of P along the a axis [Fig. 3(f)].

During the rotation of H from the angle position ▼ to ▽, P takes a nonzero value and shows a slight modulation with a local minimum at around $\theta_H = 90°, 270°$ ($H \parallel b'$). The observed behavior in that region is described by the formula

$$P_a^{\mathrm{obs}} = P_0 - \Lambda \sin^2(\theta_H \pm \theta_0). \tag{13}$$

The constant shift θ_0 (~3°) has the opposite signs (±) for clockwise and counterclockwise rotations of the H. The P_0

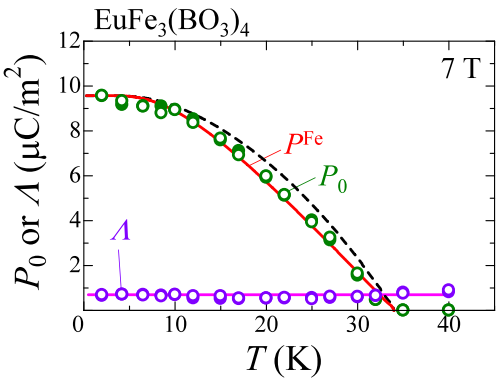

FIG. 4. (Color online) Plots of the P_0 and the Λ obtained from P-θ_H scans at various T with $\mu_0 H = 7$ T. Open (filled) circles are for the scans with clockwise (counterclockwise) rotating H. The red solid curve is the theoretical T dependence of the P_x^{Fe} computed with Eq. (8). The dashed curve is computed with Eq. (17). The pink solid line is the estimated constant value for the Λ.

term is discerned at 32 K [Fig. 3(c)], just below $T_{\mathrm{N}} \sim 34$ K, yet disappears in a paramagnetic region of 40 K [Fig. 3(d)]. These facts clearly suggest that P_0 is ascribed to the magnetic order.

The discussions in Secs. II A and II B can be applied to the single-domain region between ▼ and ▽. Assuming that the Fe antiferromagnetic order of the single domain is not modulated during the rotation of the H [Fig. 3(f)], the Fe subsystem gives rise to a constant value (P_x^{Fe}). On the other hand, we predict that the Eu ion shows the H-dependent ME response as described by Eq. (10). Substituting each component of H

$$\begin{pmatrix} H_x \\ H_y \\ H_z \end{pmatrix} = \begin{pmatrix} 0 \\ H\sin\theta_H \\ H\cos\theta_H \end{pmatrix} \tag{14}$$

into Eq. (10), we get

$$P_x^{\mathrm{Eu}} = -\lambda H^2 \sin^2\theta_H + \lambda' H^2 \sin\theta_H \cos\theta_H. \tag{15}$$

The summation of P_x^{Fe} and P_x^{Eu} gives

$$P_a = P_x^{\mathrm{Fe}} - \lambda H^2 \sin^2\theta_H, \tag{16}$$

where we put $\lambda' = 0$ since the second term in Eq. (15) was not observed in the experiment. This formula reproduces the observed phenomenon [Eq. (13)] with the assignments as $P_0 = P_x^{\mathrm{Fe}}$ and $\Lambda \sin^2\theta_H = P_x^{\mathrm{Eu}}$ except the shift $\pm\theta_0$. Since the P was obtained by integrating the time-recorded current, $\pm\theta_0$ represents some time delay of the response (e.g., domain wall motion) against the rotating H.

To confirm the above assignments, the observed behaviors are fitted by Eq. (13) at various T [black curves in Figs. 3(a)–3(d)] to plot P_0 and Λ as functions of T in Fig. 4. As described in Sec. II A, the T dependence of P_x^{Fe} can be numerically calculated by Eq. (8), where T_{N} in u [Eq. (6)] is set to 34 K corresponding to the T_{N} at 7 T [Fig. 2(a)] and τ is adjusted to reproduce the experimental value of P_0 at $T = 2$ K. The theoretical T dependence of P_x^{Fe} is shown in Fig. 4. The P_0 and P_x^{Fe} values show a quantitative agreement in the entire T range, indicating the relevance of the assignment. In contrast, Λ shows less T dependence, which is consistent with that the λ terms in Eq. (9) are ascribed to the H-induced van Vleck paramagnetism of a Eu ion. These facts suggest the availability of the theories developed in Sec. II for the interpretation of the ME response of this system. Treating the present analysis procedure as an example, we will show that the ME responses in the other two compounds can be understood by the summation of the P from Fe and R ions.

We also identified the microscopic origin of the Fe-induced P as the d-p hybridization mechanism. The exchange striction mechanism predicts the T dependence of the P_0 within the mean-field theory as

$$\tau' \left\langle \hat{S}_x^{\mathrm{Fe}} \right\rangle^2 = \tau' S^2 B_S(u)^2, \tag{17}$$

since such P is induced by correlation of neighboring spins. This formula leads to the dashed black curve in Fig. 4 by adjusting the parameter τ' to reproduce the P_0 at 2 K. There are discrepancies between the observed P_0 and Eq. (17) in the wide T range, indicating the irrelevance of this mechanism.

B. ME responses in $GdFe_3(BO_3)_4$

Next, we discuss the results of $GdFe_3(BO_3)_4$ with complex phase diagrams [Figs. 2(f) and 2(h)] under H. The similar measurements were performed in $GdFe_3(BO_3)_4$ as done for $EuFe_3(BO_3)_4$. Figures 5(a)–5(d) show the θ_H dependencies of P_a at 7 T, measured at various T. Note that in both $H \parallel b'$ [Fig. 2(f)] and $H \parallel c$ [Fig. 2(h)] the magnitude of H is far from the critical fields for the spin-flop transitions. In that

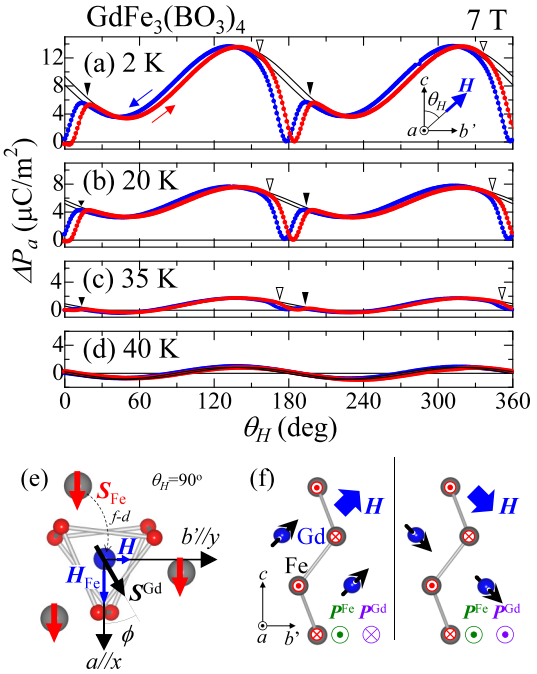

FIG. 5. (Color online) (a)–(d) P along the a axis measured at various T with $\mu_0 H = 7$ T as functions of the θ_H. The solid curves are fits with Eq. (18). (e) The schematic illustration of the magnetic structure for one of the ab planes under $H \parallel b'$. (f) The schematic illustrations of the magnetic structures under a rotating H. Green (purple) ⊙ and ⊗ show the direction of the P induced by the Fe (Gd) subsystem.

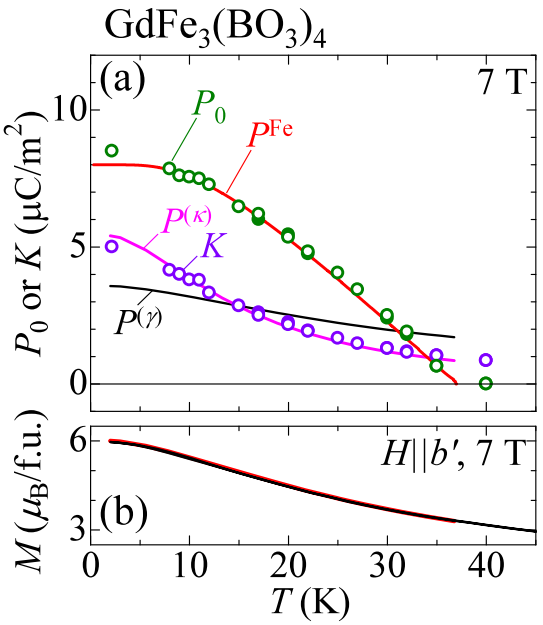

FIG. 6. (Color online) (a) Plots of the P_0 and the K obtained from P-θ_H scans at various T with $\mu_0 H = 7$ T. Open (filled) circles are for the scans with clockwise (counterclockwise) rotating H. The red solid curve is the theoretical T dependence of the $P_x^{\rm Fe}$, computed with Eq. (8). The pink (black) solid curve is the computed T dependence of the $P^{(\kappa)}$ ($P^{(\gamma)}$). (b) The black solid curve is the T dependence of the M measured at 7 T under $H \parallel b'$. The red solid curve is the theoretical T dependence of the M, computed by Eq. (28).

case, the Fe spins are expected to lie along the ab plane during the rotation of H.

At 2 K and 20 K [Figs. 5(a) and 5(b)], the behaviors of P_a around $\theta_H = 0°, 180°$ ($H \parallel c$) are quite similar to those of $EuFe_3(BO_3)_4$; as H is inclined towards the b' axis, the P_a steeply emerges signaling the reorientation of the Fe spins to the a axis. Such V-shaped responses between the two θ_H positions, a open triangle ($\triangledown$) and a closed triangle ($\blacktriangledown$), are observed at up to 35 K and disappear at above 40 K [Figs. 5(c) and 5(d)], which suggests that the Fe-spin ordering survives at around $T_{\rm N} = 37$ K even under $\mu_0 H = 7$ T.

The P_a shows a characteristic angular dependence in a region from $\blacktriangledown$ to $\triangledown$ through $\theta_H = 90°$, which is described by

$$P_a^{\rm obs} = P_0 - K \sin 2(\theta_H \pm \theta_0). \tag{18}$$

The fitted curves are shown with black lines in Figs. 5(a)–5(d). With the same measurements at various T we obtained P_0 and K, which were plotted as functions of T in Fig. 6(a). The numerical computation of the T dependence of $P_x^{\rm Fe}$ using Eq. (8) gives a red curve in Fig. 6(a), where $T_{\rm N}$ in u [Eq. (6)] is set to 37 K and τ is adjusted so as to reproduce the P_0 at 5 K. The calculated $P_x^{\rm Fe}$ shows a good agreement with the P_0 in the entire T region, which suggests the P_0 term originating from the Fe subsystem. On the other hand, the second term in Eq. (18) is quite different from that of Eq. (13) observed in $EuFe_3(BO_3)_4$, which indicates that the K term comes from the Gd ions. To confirm the above assignment we shall reproduce the $P_a^{\rm obs}$ described by Eq. (18) by the summation of the $P_x^{\rm Fe}$ and the $P_x^{\rm Gd}$ with a model of the angular dependence of the magnetic structure of each subsystem.

According to the previous antiferromagnetic resonance studies [17,18], the magnetic structure for one of the ab planes of $GdFe_3(BO_3)_4$ under $H \parallel b'$ can be schematically illustrated as in Fig. 5(e). Fe spins in one of the sublattices align perpendicular to H, whereas a Gd spin is canted by ϕ from the a axis towards the b' axis due to the balance between the external H and the f-d molecular field from the Fe spins ($H_{\rm Fe}$). Hereafter, we neglect a slight canting of the Fe spins towards the b' axis. Let us consider the case when the H is rotated around the a axis; the Fe spins show less modification from polarizing along the a axis and contributes to the P_a by a constant value $P_x^{\rm Fe}$, whereas the Gd spin rotates around the a axis towards H [Fig. 5(f)], keeping the canting angle from the a axis by ϕ. The model for the angular dependence of the Gd spin is introduced as

$$\boldsymbol{S}^{\rm Gd} = \begin{pmatrix} S_{\rm Gd}\cos\phi \\ S_{\rm Gd}\sin\phi\sin\theta_H \\ S_{\rm Gd}\sin\phi\cos\theta_H \end{pmatrix}, \tag{19}$$

where we ignore the anisotropy of the Gd spin by taking the azimuth angle θ as θ_H. Note that the Gd spins in the other sublattice can be described by replacing the angle ϕ of Eq. (19) with the term $180° - \phi$ because the Gd spin is canted from the a axis due to the f-d molecular field ($-\boldsymbol{H}_{\rm Fe}$) from the other sublattice of the Fe spins.

Here, we treat the spin moment as a classic vector to skip the statistical averages of the operators. Substituting Eq. (14) and (19) into Eq. (11), we get

$$\begin{aligned} P_x^{\rm Gd} &= \kappa' S_{\rm Gd}^2(\cos^2\phi - \sin^2\phi\sin^2\theta_H) \\ &\quad + \kappa S_{\rm Gd}^2 \sin^2\phi \sin\theta_H\cos\theta_H - \gamma' S_{\rm Gd} H \sin\phi\sin^2\theta_H \\ &\quad + (\gamma+\gamma'') S_{\rm Gd} H \sin\phi\sin\theta_H\cos\theta_H. \end{aligned} \tag{20}$$

This is sufficient to know the allowed form of the $P_x^{\rm Gd}$ as a function of θ_H. We can check that the other sublattice of the Gd spins gives the same formula because it is invariant under the change of ϕ to $180° - \phi$. Since we did not observe the angular dependence of $\sin^2\theta_H$ type, we put κ' and γ' zero to get

$$P_x^{\rm Gd(cl)} = \tfrac{1}{2}\left[\kappa S_{\rm Gd}^2 \sin^2\phi + (\gamma+\gamma'') S_{\rm Gd} H \sin\phi\right] \sin 2\theta_H, \tag{21}$$

where the superscript (cl) indicates the classical treatment of the spins. Since the terms in brackets [ ] are assumed to be constant during the rotation of H for each sublattice, the summation of $P_x^{\rm Fe}$ and $P_x^{\rm Gd(cl)}$ [Eq. (21)] successfully reproduces the observed feature [Eq. (18)] except the shift $\pm\theta_0$; this is presumably due to the same origin as mentioned in Sec. IV A.

As can be seen from Eq. (21), the $P_x^{\rm Gd}$ is composed of the two terms: a spin-induced spontaneous P ($\propto\kappa$) and an H-linear P [$\propto (\gamma+\gamma'')$]. To know their ratio we focus on the T dependence of K. The above treatment of the Gd spin as a classical vector is not applicable to this; instead, we need to calculate the statistical averages of the spin operators in Eq. (11) to deduce the formula for the $P_x^{\rm Gd}$ as a function of T.

We take the following Hamiltonian $\hat{\mathcal{H}}_{\rm Gd}$ for a Gd spin ($\hat{\boldsymbol{S}}^{\rm Gd}$) under a rotating $\boldsymbol{H}$ [Eq. (14)],

$$\hat{\mathcal{H}}_{\rm Gd} = g\mu_{\rm B}(\boldsymbol{H} + \boldsymbol{H}_{\rm Fe}) \cdot \hat{\boldsymbol{S}}^{\rm Gd}, \tag{22}$$

where $\boldsymbol{H}_{\rm Fe}$ is the f-d exchange field from the Fe subsystem. The single-site anisotropy, the exchange interaction between Gd ions, and the dipole-dipole interaction are not included here, since all of them are negligible compared with the terms in Eq. (22).

Within this Hamiltonian the method described in the Appendix is applicable for calculation of the statistical average of polynomials of operators because Eq. (22) belongs to the Hamiltonian in Eq. (A1) with the effective field $\boldsymbol{H}_{\rm eff}$,

$$\boldsymbol{H}_{\rm eff} = \boldsymbol{H} + \boldsymbol{H}_{\rm Fe} = \begin{pmatrix} H_{\rm Fe} \\ H\sin\theta_H \\ H\cos\theta_H \end{pmatrix}. \tag{23}$$

Substitution of Eq. (14), (A6), and (A8) into Eq. (11) gives a quantum mechanical formula (q) of the $P_x^{\rm Gd}$ as follows

$$P_x^{\rm Gd(q)} = \frac{3\kappa}{4}\sin^2\phi\sin 2\theta_H J^2\left[B_J^2(v) + B_J'(v) - \frac{J+1}{3J}\right] + \frac{1}{2}(\gamma+\gamma'')H\sin\phi\sin 2\theta_H J B_J(v), \tag{24}$$

where $J = \frac{7}{2}$. Here, we define the first and second terms of Eq. (24) as $P^{(\kappa)}\sin 2\theta_H$ and $P^{(\gamma)}\sin 2\theta_H$, respectively. The parameters $P^{(\kappa)}$ and $P^{(\gamma)}$ are the quantities to be compared with the experimental parameter K. The terms proportional to κ' and γ' are omitted since the corresponding angular dependencies do not appear in the experiment. Note that Eq. (24) expresses not only the same angular dependence as Eq. (21) but also the functional form with respect to T and H through v, ϕ, and $H_{\rm Fe}$, which are given by

$$v = \frac{g\mu_{\rm B}J\sqrt{H_{\rm Fe}^2 + H^2}}{k_{\rm B}T}, \tag{25}$$

$$\phi = \tan^{-1}\frac{H}{H_{\rm Fe}}, \tag{26}$$

$$H_{\rm Fe} = h\frac{\langle\hat{S}_x^{\rm Fe}\rangle}{S}. \tag{27}$$

For the T dependence of $P^{(\kappa)}$ and $P^{(\gamma)}$, Eqs. (6) and (7) are used to compute the T dependence of $\langle\hat{S}_x^{\rm Fe}\rangle$ and $H_{\rm Fe}$ is taken as 62 kOe at $T = 0$ ($h = 62$ kOe); this value of $H_{\rm Fe}$ is similar to the one (~70 kOe) estimated in Ref. [28]. We show the calculated T dependencies of them in Fig. 6(a), where the parameters κ, γ, and γ'' are adjusted so as to reproduce the K at 15 K. The $P^{(\kappa)}$ alone shows a satisfactory agreement in the entire T range while the $P^{(\gamma)}$ showing merely gentle T dependence. While the K term should, in principle, be expressed by the summation of $P^{(\kappa)}$ and $P^{(\gamma)}$ with some ratio, we can safely conclude that the $P^{(\kappa)}$ term dominantly contributes to the Gd-induced P, and that the $P^{(\gamma)}$ term only contributes to it by a minor amount.

To check the validity of the value of h, T dependence of M was measured under $H \parallel b'$ of 7 T [Fig. 6(b)]. For the model of M, we take the form

$$M = \chi_{\rm Fe}H + g\mu_{\rm B}J\sin\phi B_J(v). \tag{28}$$

The first term is the T-independent M from the antiferromagnetic Fe subsystem. The second term is the contribution from Gd spins, which is assumed to be canted by ϕ from the a axis [Fig. 5(e)]. Equation (28) is related with h through v and ϕ. We choose the value of $\chi_{\rm Fe}$ as $\chi_{\rm Fe}H = 0.8\mu_{\rm B}$ at 7 T, which is determined from the magnetic susceptibility of $YFe_3(BO_3)_4$ [10]. The red curve in Fig. 6(b) shows the calculated T dependence of M. We successfully fit the experimental M-T curve with the theoretical one, which justifies the choice of fit h.

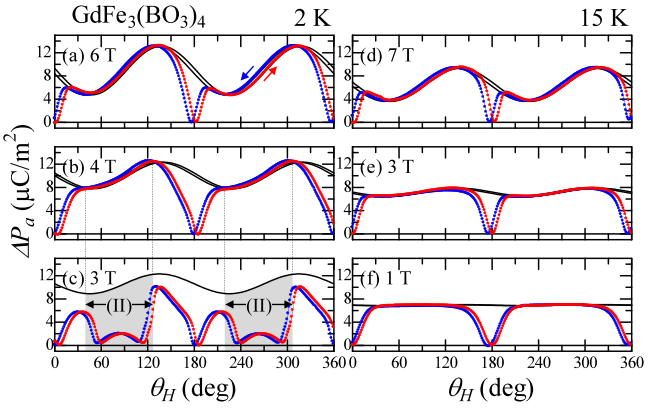

FIG. 7. (Color online) (a)–(f) P along the a axis measured with various H and T as functions of the θ_H. The solid curves are fits with Eq. (18). In (c), the solid curve is a fictitious P-θ_H curve by Eq. (18); P_0 and K were estimated appropriately from the data in Fig. 8(a).

Since $GdFe_3(BO_3)_4$ has complex phase diagrams under H, it is necessary to check the range of the applicability of the above discussion. The P-θ_H scans were performed under various H [Figs. 7(a)–7(f)]. At 2 K, the regime of Eq. (18) is clearly observed down to 4 T [Figs. 7(a) and 7(b)], while at 3 T [Fig. 7(c)] a sudden drop of P_a is observed in the hatched regions, signaling the transition to phase II [Fig. 2(g)]. Indeed, the magnitude of H is lower than the critical $\mu_0 H$ (~3.7 T) for the transition to phase III [Fig. 2(f)] under $H \parallel b'$ ($\theta_H = 90°$). A modulation of P_a in the hatched region may be due to the deviation of the magnetic structure from that illustrated in Fig. 2(g) by H. Figures 7(d)–7(f) show the corresponding data at 15 K. Equation (18) is observed to be applicable with changing the oscillation amplitude K as H is decreased down to 1 T, indicating that the picture of the magnetic structure shown in Fig. 5(f) holds good even under such a magnitude of H.

The obtained P_0 and K at 2 K and 15 K were plotted as functions of H in Fig. 8(a). At 15 K, the P_0 is almost independent of H, which is consistent with the assumption that the canting of Fe spins towards H may be ignored. On the other hand, at 2 K the P_0 decreases as H increases, which suggests a slight modification on the Fe subsystem probably due to the f-d molecular field. We also shows the H dependencies of P_a under $H \parallel b'$, which were measured at 15 K and 2 K [Fig. 8(a)]. The P_a at 15 K shows good agreement with P_0 ($=P_x^{\rm Fe}$), which is consistent with the fact that the Gd-induced P ($\propto\sin 2\theta_H$) is

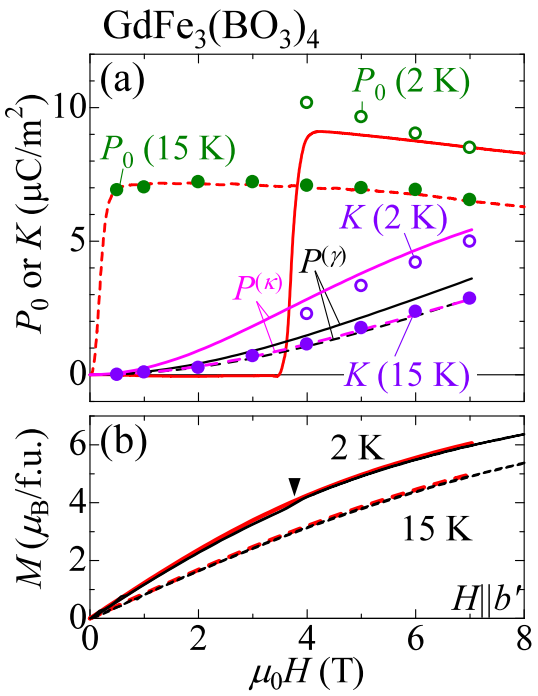

FIG. 8. (Color online) (a) Plots of the P_0 and the K as functions of the H. The red solid (dashed) curve is the H dependence of the ΔP_a at 2 K (15 K) under $H \parallel b'$. The pink solid (dashed) curve and the black solid (dashed) curve are the theoretical H dependencies of the $P^{(\kappa)}$ and the $P^{(\gamma)}$ at 2 K (15 K), respectively. (b) The black solid (dashed) curve is the H dependence of the M measured at 2 K (15 K) under $H \parallel b'$. A black triangle indicates the anomaly for the spin-flop transition from phase II to III. The red solid (dashed) curve is the theoretical H dependence of the M, computed by Eq. (28) with $T = 2$ K (15 K).

absent under $H \parallel b'$ ($\theta_H = 90°$). While the agreement between the P-H curve and the P_0 at 2 K is almost good, we discern a slight discrepancy at a lower field region (~4 T). This seems to come from the misestimation of P_0 in the fitting of the P-θ_H curves with Eq. (18) because there is a deviation of the fitted curve from the observed P in Fig. 7(b). Since H of 4 T is just above the critical field between phases II and III under $H \parallel b'$ [Fig. 2(f)], the magnetic structure under rotating H should be slightly different from the currently applied picture [Fig. 5(f)]. It was theoretically suggested there is an "angular phase" with Fe spins rotated from the ab plane towards the c axis at around the critical field for $H \perp c$ [17].

Figure 8(a) shows the H dependencies of $P^{(\kappa)}$ and $P^{(\gamma)}$ calculated with the corresponding terms in Eq. (24), where the same parameters κ, γ, γ'', and h are used for the discussion on the T dependence of the K. Again, the $P^{(\kappa)}$ alone shows a quantitative agreement for the H dependencies of K at both 2 K and 15 K, ensuring that the spin-induced spontaneous P [$\propto \kappa \langle \hat{S}_y \hat{S}_z \rangle$] is relevant as the ME origin of the Gd ion. As for the $P^{(\gamma)}$, although it well reproduces the K at 15 K because the $\gamma + \gamma''$ is chosen to reproduce the K at 15 K with $\mu_0 H = 7$ T in Fig. 6(a), it does not show agreement with the K at 2 K. This result again indicates that the $P^{(\gamma)}$ term cannot be the main origin of K by itself, and possibly contributes to it with a small amount besides the dominantly contributing $P^{(\kappa)}$ term. The validity of the choice of h is also checked by the M-H curves. Figure 8(b) shows the H dependencies of M (black lines) under $H \parallel b'$ at 2 K and 15 K. A small anomaly is indicated by a black triangle (▼), which is related with the spin-flop transition from phase II to III [27]. The theoretical curves at corresponding T are shown in the same figure by red curves, which were calculated by Eq. (28) with the same parameters $\chi_{\rm Fe}$ and h as in fitting the M-T curve. The agreements between the observation and the theories are excellent at 15 K and at 2 K for H higher than the critical field, confirming the relevance of the model for the magnetic structure.

Note that the Gd component of the P ($\propto \sin 2\theta_H$) does not contribute to the P_a within usual P-H measurements under $H \parallel c$ ($\theta_H = 0°$) and $H \parallel b'$ ($\theta_H = 90°$). We can easily confirm by Eq. (11) that it is also the case for $H \parallel a$, which is the measurement condition in Ref. [8]. With the measurement of the angular dependence of the P, we succeeded in unraveling the role of the Gd subsystem in the ME response, which would be hard to know by the P-H scans with the H along certain crystal axes.

C. ME responses in $TbFe_3(BO_3)_4$

We further investigate the ME responses in $TbFe_3(BO_3)_4$, in which the Tb moment with the strong Ising anisotropy is expected to cause a unique θ_H dependence of P. The P along the a axis was measured at 2 K with H of 7 T rotating around the a axis [Fig. 9(a)]. In the condition of $H \parallel c$ ($\theta_H = 0°, 180°$), the magnitude of H is sufficiently higher than the critical field (~3.5 T), assuring the transition to the metamagnetic phase II [Fig. 2(c)]. When the H rotates clockwise [the red curve in Fig. 9(a)] from $\theta_H = 0°$ towards the b' axis, the P shows a slight jump to a positive value at the angle position indicated by a closed triangle (▼). According to the preceding results in $EuFe_3(BO_3)_4$ and $GdFe_3(BO_3)_4$, this is assigned to the reorientation of the Fe spins along the a axis to induce the $P_x^{\rm Fe}$ [Fig. 9(e)]. As H is further inclined towards the b' axis, P_a decreases to show a negative value suggesting that the Tb moment as well as the Fe spins contributes to the P.

This regime ends at the angle position indicated by an open diamond (◇) with a sudden disappearance of P_a. The critical angle is about $\theta_H = 60°$, at which the c component of H coincides with the critical field (~3.5 T). Since Zeeman energy of the Tb moment with large Ising anisotropy drives the metamagnetic transition [16], the crystal undergoes the collinear antiferromagnetic order with the magnetic moments along the c axis [Fig. 9(f)]. A small P is discerned in the corresponding region, which may be a second-order ME effect due to a slight modulation of the Fe spins by H. Corresponding P was observed in a former study with the P-H scan under $H \parallel a$ [9]. At the angle indicated by a closed diamond (◆), the P_a shows a sudden change signaling the return to the metamagnetic phase [Fig. 9(g)]. As H rotates towards the c axis ($\theta_H = 180°$), the P_a again shows the characteristic angular dependence until a drop at the angle of an open triangle (▽) indicating a breakdown of the single magnetic domain.

In the θ_H regions of ▼-◇ and ◆-▽, both the Fe spins along the a axis and the Tb moments along the c axis contribute to

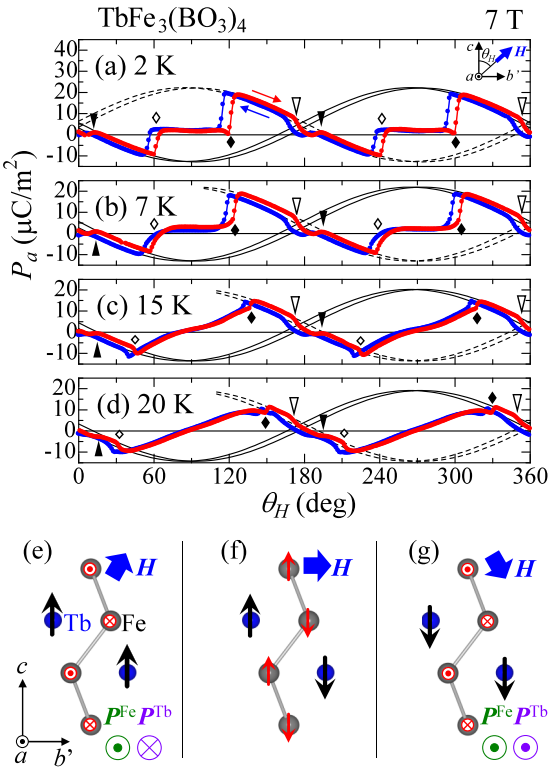

FIG. 9. (Color online) (a)–(d) P along the a axis measured at various T with $\mu_0 H = 7$ T as functions of the θ_H. The solid and dashed curves are fits with Eq. (29). (e)–(g) The schematic illustrations of the magnetic structures under a rotating H. Green (purple) ⊙ and ⊗ show the direction of the P induced by the spins (magnetic moments) at the Fe (Tb) subsystem.

P. The angular dependence of P_a is well described by

$$P_a^{\rm obs} = P_0 \mp \Gamma \sin(\theta_H \pm \theta_0), \tag{29}$$

where the parameter Γ is taken as positive, the sign $-(+)$ in front of the Γ is for the P_a around $\theta_H = 0^\circ$ (180°), and the constant shift $-(+)\theta_0$ is for the clockwise (counterclockwise) P-θ_H scan. The presence of the constant shift θ_0 in Eq. (29) may be due to the same reason mentioned in Sec. IV A. The fitted curves are shown by solid and dashed lines in Fig. 9(a).

To reproduce the behavior described by Eq. (29) except $\pm\theta_0$, we shall apply the phenomenological theory developed in Secs. II A and II B, according to which the first term of Eq. (29) corresponds to the Fe magnetic order ($P_x^{\rm Fe}$) and the second term originates from the Tb moment under H [Eq. (12)]. Substituting Eq. (14) into Eq. (12) gives

$$P_x^{\rm Tb} = \gamma \langle \hat{S}_z^{\rm Tb} \rangle H \sin\theta_H, \tag{30}$$

which reproduces the second term of Eq. (29) if $\langle \hat{S}_z^{\rm Tb} \rangle$ is θ_H independent except its sign. When we define γ as negative, the proportionality between $\langle \hat{S}_z^{\rm Tb} \rangle$ and the Tb-induced M ($M_{\rm Tb}$) gives $\gamma \langle \hat{S}_z^{\rm Tb} \rangle < 0$ around $\theta_H = 0^\circ$ ($M_{\rm Tb} > 0$) and $\gamma \langle \hat{S}_z^{\rm Tb} \rangle > 0$ around $\theta_H = 180^\circ$ ($M_{\rm Tb} < 0$); this coincides with the sign ($\mp$) in front of the Γ. While the θ_H dependence of $\langle \hat{S}_x^{\rm Tb} \rangle$ ($\propto M_{\rm Tb}$) is possibly present, it is assumed to be constant in the regions of ♦-▽ and ◇-▼, because the Ising nature of the Tb moment

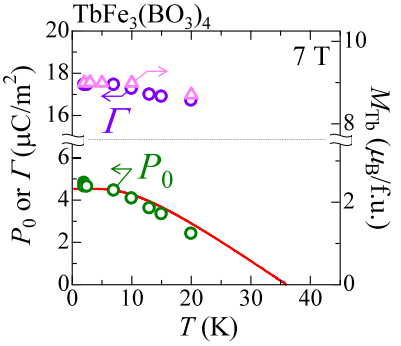

FIG. 10. (Color online) Plots of the P_0, the Γ and the magnetic moment of a Tb ion ($M_{\rm Tb}$) as functions of T. Open (filled) circles are for the scans with clockwise (counterclockwise) rotating H of 7 T. The red solid curve is the theoretical T dependence of the $P_x^{\rm Fe}$ computed with Eq. (8).

keeps the $M_{\rm Tb}$ fully polarized until the c component of the H becomes less than the critical H.

This scenario is supported by the feature of the M-H curve under $H \parallel c$. In $H \parallel c$, the H dependence of the M in the metamagnetic phase II ($H \gtrsim 3.5$ T) at $T = 4.2$ K can be well reproduced by the formula

$$M = \chi H + M_0, \tag{31}$$

with the values of $\chi \sim 1 \times 10^{-5}$ ($\mu_{\rm B}$/Oe) and $M_0 \sim 9$ ($\mu_{\rm B}$) [16]. The first and second terms typically represent the contributions from the antiferromagnetic Fe spin order and the Tb moment of $g \sim 18$, respectively. The H-independent M_0 ($\sim M_{\rm Tb}$) suggests that the Tb moment is fully polarized above the critical field; thus, we can assume the $\langle \hat{S}_x^{\rm Tb} \rangle$ is also independent of θ_H in the regions of ♦-▽ and ◇-▼.

To confirm the above assignment that $P_0 = P_x^{\rm Fe}$ and $\mp\Gamma \sin(\theta_H) = P_x^{\rm Tb}$, the P-θ_H scans were performed at various T with $\mu_0 H = 7$ T. The representative results are shown in Figs. 9(a)–9(d). Similar features as discussed above are observed up to $T = 20$ K. We obtained the values of P_0 and Γ by fitting the data by Eq. (29) and plotted them as functions of T in Fig. 10. The calculated T dependence of the $P_x^{\rm Fe}$ is shown by the red curve in Fig. 10, where we used $T_{\rm N} = 36$ K in u [Eq. (6)] corresponding to the transition T under $H \parallel c$ of 7 T [Fig. 2(c)] and adjusted τ so as to reproduce the P_0 at 2 K. The agreement of P_0 and $P_x^{\rm Fe}$ is good except a slight discrepancy at 20 K, which may suggest some deviation of the T dependence of the Fe spins from Brillouin function due to the presently ignored f-d coupling. For clarification, the T dependence of the Fe-sublattice magnetization under H should be estimated by a neutron scattering technique.

To prove the equation

$$\mp\Gamma = \gamma \langle \hat{S}_x^{\rm Tb} \rangle H, \tag{32}$$

we need the T dependence of $\langle \hat{S}_x^{\rm Tb} \rangle$, which can be estimated from the magnitude of $M_{\rm Tb}$ through the relationship $M_{\rm Tb} \propto \langle \hat{S}_x^{\rm Tb} \rangle$. The H dependence of M was measured under $H \parallel c$ at various T and the H-linear term [χH in Eq. (31)] was subtracted from the M-H curve for the estimation of $M_{\rm Tb}$ at 7 T. The obtained values are plotted as a function of T in

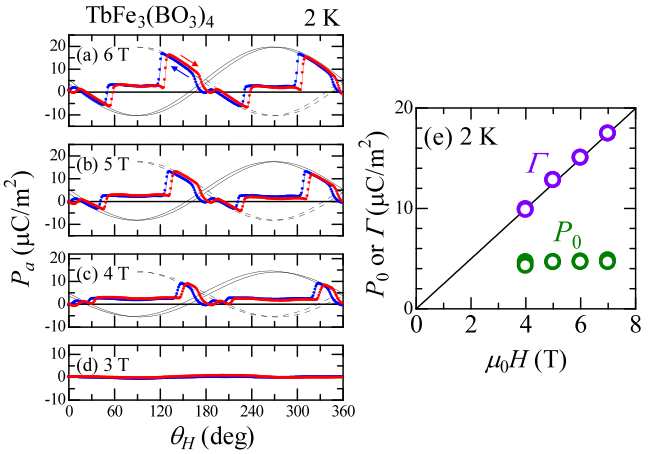

FIG. 11. (Color online) (a)–(d) P along the a axis at 2 K with various H as functions of the θ_H. The solid and dashed curves are fits with Eq. (29). (e) Plots of the P_0 and the Γ as functions of the H. The solid line is a guide for the eyes.

Fig. 10. The T dependencies of Γ and $M_{\rm Tb}$ are scaled with each other ($\Gamma \propto M_{\rm Tb}$), indicating the validity of Eq. (32).

We further performed the P-θ_H scans at 2 K with various magnitudes of H [Figs. 11(a)–11(d)]. Down to 4 T slightly above the critical H for the metamagnetic transition, we observe the regime which can be described by Eq. (29), while at 3 T below the critical field the P hardly shows the angular dependence, being consistent with a tiny P observed under $H \parallel a$ in a former study [9]. The fitted curves are shown by solid and dashed lines in Figs. 11(a)–11(c). The obtained values P_0 and Γ are plotted as functions of the H in Fig. 11(e). P_0 is almost constant with respect to the magnitude of H, indicating the modification of the antiferromagnetic order of the Fe spins by H is negligible; by contrast, the Γ is clearly proportional to H, which confirms Eq. (32) with the assumption that $\langle \hat{S}_x^{\rm Tb} \rangle$ is H independent.

In a previous study on $TbFe_3(BO_3)_4$ a small jump of P_a at the metamagnetic transition under $H \parallel c$ was reported [9]. It was suggested that the ME domains were not compensated due to the uncontrollable misalignment of H. In the present study we controlled the canting angle of the H from the c axis and successfully revealed that the canted H not only arranges the antiferromagnetic Fe domains with spontaneous P but also induces the P from the Tb ion. We again confirm that the measurement of the angular dependence of P is useful for the understanding of the magnetic-ion resolved origins of the ME response.

D. Discussion

We briefly discuss the microscopic origins of the R-induced P. In Sec. II B, we assume that the spin- and the H-induced P from a R ion can be written by Eq. (9). This form of P can be justified by considering the modification of the (pseudo)spin Hamiltonian $\hat{\mathcal{H}}$ under E, whose physics is common to the E effect in paramagnetic resonance [42,43]. Considering the effect of E applied on a crystal, the electronic structure and/or the lattice structure are modulated to induce the additional term $\hat{\mathcal{H}}_E$ to $\hat{\mathcal{H}}$ as follows:

$$\hat{\mathcal{H}}_E = -\sum_{ijk} E_i(\kappa_{ijk}\hat{S}_j\hat{S}_k + \gamma_{ijk}\hat{S}_j H_k). \tag{33}$$

The respective terms correspond to the E-induced magnetic anisotropy and a shift of the g factor, which were used to account for the shift of the resonance of several kinds of R^{3+} ions doped in $CaWO_4$ and some halides [44,45]. On the other hand, in the context of the ME responses of R ions in magnets we can deduce P by differentiating $\hat{\mathcal{H}}_E$ by E_i ($P_i = -\frac{\partial \langle \hat{\mathcal{H}}_E \rangle}{\partial E_i}$), which gives the same formula of Eq. (9) except the λ terms, which may correspond to the E effect of van Vleck paramagnetism.

In fact, it was observed the splitting of the resonance parameters for the magnetic anisotropy by the application of E in $LaCl_3$:Gd^{3+} [46], which is of the order of 10^{-4} cm^{-1} for $|E| = 1.7 \times 10^7$ V/m. By taking the lattice constant several angstroms the observed value corresponds to the $P \sim 1$ μC/m^2, which is comparable to the Gd-induced P (~ 5 μC/m^2) revealed in this work. While the estimation of the parameters in Eq. (33) were reported considering the hybridization of the $4f$ and $5d$ orbitals via a noncentrosymmetric crystal field with a distortion of the surrounding ligands [47,48], quantitative agreements have not been achieved. A more precise method to estimate the expected ME responses based on the detailed knowledge of the electronic wave function and the crystal structure would be needed.

V. CONCLUDING REMARKS

We have investigated the ME responses in three R ferroborates with R = Eu, Gd, and Tb. We focused on the respective magnetic subsystems and theoretically discussed the ME functionality of the individual magnetic ions. Considering their local symmetry and features of ground-state multiplets, the expressions for respective contributions to P were deduced. We measured P along the a axis with rotating H around the a axis and successfully reproduced most of the observed behaviors as the summation of P from each magnetic subsystem.

In $EuFe_3(BO_3)_4$, a collinear antiferromagnetic ordering of Fe spins yields an almost θ_H-independent P, which is overlapped by the smaller P derived from paramagnetic Eu ions. In both $GdFe_3(BO_3)_4$ and $TbFe_3(BO_3)_4$, the Fe-induced spontaneous P is accompanied by θ_H-dependent highly anisotropic P, which characterizes the ME property of the R magnetic moment. A spin on a Gd ion smoothly rotates along H to generate a spontaneous P, which is analogous to the spin-induced P due to the d-p hybridization mechanism [33] in transition-metal compound multiferroics. The Ising nature of a Tb moment confines itself along the c axis resulting in a linear ME effect under H.

The observed ME responses can be decomposed into the components from the respective magnetic subsystems. The theoretical calculation taking account of the atomic origins of the respective components can account for the observed features. In particular, the measurement of the angular dependence of P is useful to understand the ME properties with plural magnetic subsystems.

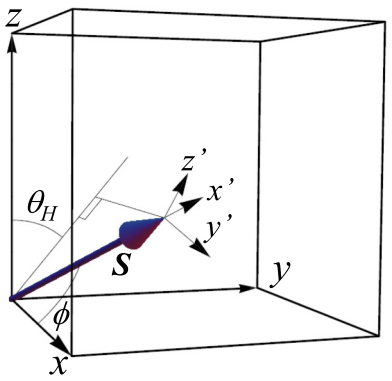

FIG. 12. (Color online) The definitions of coordinates for a spin moment $\boldsymbol{S}$.

In this paper, we concentrated on the three R ferroborates, which are characterized by their mutually distinctive magnetic properties. Actually, they can be considered as typical compounds among the $R\mathrm{Fe}_3(\mathrm{BO}_3)_4$ family. Their magnetic ground states can be classified into three types: an easy-plane type such as R = Y, Nd, Sm, Eu, and Er; an easy-axis type such as R = Pr, Tb, and Dy; and an intermediate type such as R = Gd and Ho, which are characterized by a spin-reorientation transition from the easy-plane to the easy-axis type at T_{SR}. We believe that similar behaviors can be observed in these ferroborates, to which the analyses as developed in this paper are generically applicable.

ACKNOWLEDGMENTS

We thank Y. Tokunaga, T. Masuda, M. Soda, Y. Hirata, and Y. Motome for enlightening discussions. This work was partly supported by a Grant-in-Aid for Scientific Research (Grant No. 24224009) from the MEXT of Japan, and the FIRST Program of JSPS.

APPENDIX: CALLEN AND CALLEN TECHNIQUE

H. B. Callen and E. Callen worked on a theory of the magnetic anisotropy and developed a technique for calculation of the statistical average of polynomials of the lth degree $[\mathscr{S}_l(\hat{\boldsymbol{S}})]$ in the components of spin operators $(\hat{\boldsymbol{S}})$ [49]. Their mathematical technique is of key importance for the computation of the terms like $\langle \hat{S}_y \hat{S}_z \rangle$ in Eq. (11). Here, we review the points of their theory.

Let us consider a spin moment $\boldsymbol{S}$ with the quantum number J described by a spin Hamiltonian in the form

$$\hat{\mathcal{H}} = g\mu_{\mathrm{B}} \boldsymbol{H}_{\mathrm{eff}} \cdot \hat{\boldsymbol{S}}, \tag{A1}$$

where $\boldsymbol{H}_{\mathrm{eff}}$ is an effective magnetic field such as a summation of $\boldsymbol{H}$ and a molecular field. We define the spherical coordinates ϕ and θ_H for the $\boldsymbol{S}$ (Fig. 12), which is polarized along $\boldsymbol{H}_{\mathrm{eff}}$. The $\mathscr{S}_l(\hat{\boldsymbol{S}})$ is conveniently written as a linear combination of spherical harmonics,

$$\mathscr{S}_l(\hat{\boldsymbol{S}}) = \sum_m a_l^m Y_l^m(\hat{\boldsymbol{S}}). \tag{A2}$$

Here, we introduce new Cartesian coordinates (x', y', and z'), where the x' axis is parallel to the spin moment (Fig. 12). $\hat{\boldsymbol{S}}$ can be reexpressed by the new operators $\hat{\boldsymbol{S}}'$ defined on the new coordinates. The transformation among them is expressed as

$$\begin{pmatrix} \hat{S}_x \\ \hat{S}_y \\ \hat{S}_z \end{pmatrix} = \begin{pmatrix} \cos\phi & 0 & -\sin\phi \\ \sin\phi\sin\theta_H & \cos\theta_H & \cos\phi\sin\theta_H \\ \sin\phi\cos\theta_H & -\sin\theta_H & \cos\phi\cos\theta_H \end{pmatrix} \begin{pmatrix} \hat{S}'_{x'} \\ \hat{S}'_{y'} \\ \hat{S}'_{z'} \end{pmatrix}. \tag{A3}$$

Then, we get a new expression for $\mathscr{S}_l$ with the operator $\hat{\boldsymbol{S}}'$:

$$\mathscr{S}_l(\hat{\boldsymbol{S}}') = \sum_m a_l^m \sum_{m'} b_l(m,m') Y_l^{m'}(\hat{\boldsymbol{S}}'), \tag{A4}$$

where $b_l(m,m')$ can be expressed by $\cos\phi$, $\sin\theta_H$, etc., and the spherical harmonics $Y_l^{m'}(\hat{\boldsymbol{S}}')$ is defined with the principal axis along the x' axis.

Since $\hat{\mathcal{H}}$ is cylindrically symmetric around the x' axis, the statistical average $\langle Y_l^{m'}(\hat{\boldsymbol{S}}') \rangle$ is zero unless $m' = 0$. Thus,

$$\begin{aligned} \langle \mathscr{S}_l(\hat{\boldsymbol{S}}) \rangle &= \sum_m a_l^m \sum_{m'} b_l(m,m') \langle Y_l^{m'}(\hat{\boldsymbol{S}}') \rangle \\ &= \sum_m a_l^m b_l(m,0) \langle Y_l^0(\hat{\boldsymbol{S}}') \rangle. \end{aligned} \tag{A5}$$

Application of the formula to $l = 1$ and 2 gives

$$\langle \hat{\boldsymbol{S}} \rangle = \begin{pmatrix} J\cos\phi \\ J\sin\phi\sin\theta_H \\ J\sin\phi\cos\theta_H \end{pmatrix} B_J(v), \tag{A6}$$

$$\begin{aligned} \langle \hat{S}_x^2 - \hat{S}_y^2 \rangle &= \frac{1}{2}(\cos^2\phi - \sin^2\phi\sin^2\theta_H) \langle 3\hat{S}_{x'}'^2 - (J+1)J \rangle \\ &= \frac{3}{2}(\cos^2\phi - \sin^2\phi\sin^2\theta_H) J^2 \\ &\quad \times \left[B_J^2(v) + B_J'(v) - \frac{J+1}{3J} \right], \end{aligned} \tag{A7}$$

$$\begin{aligned} \langle \hat{S}_y \hat{S}_z \rangle &= \frac{1}{4}\sin^2\phi\sin 2\theta_H \langle 3\hat{S}_{x'}'^2 - (J+1)J \rangle \\ &= \frac{3}{4}\sin^2\phi\sin 2\theta_H J^2 \left[B_J^2(v) + B_J'(v) - \frac{J+1}{3J} \right], \end{aligned} \tag{A8}$$

where v and ϕ are given as

$$v = \frac{g\mu_{\mathrm{B}} J H_{\mathrm{eff}}}{k_{\mathrm{B}} T}, \tag{A9}$$

$$\phi = \tan^{-1} \frac{H_{\mathrm{eff}x}}{\sqrt{H_{\mathrm{eff}y}^2 + H_{\mathrm{eff}z}^2}}. \tag{A10}$$

[1] L. D. Landau and E. M. Lifshitz, *Electrodynamics of Continuous Media* (Pergamon, Oxford, 1959).
[2] I. E. Dzyaloshinskii, Sov. Phys. JETP **10**, 628 (1960).
[3] D. N. Astrov, Sov. Phys. JETP **11**, 708 (1960).
[4] T. Kimura, T. Goto, H. Shintani, K. Ishizaka, T. Arima, and Y. Tokura, Nature (London) **426**, 55 (2003).
[5] H. Murakawa, Y. Onose, S. Miyahara, N. Furukawa, and Y. Tokura, Phys. Rev. Lett. **105**, 137202 (2010).
[6] S.-W. Cheong and M. Mostovoy, Nat. Mater. **6**, 13 (2007).
[7] Y. Tokura and S. Seki, Adv. Mater. **22**, 1554 (2010).
[8] A. K. Zvezdin, S. S. Krotov, A. M. Kadomtseva, G. P. Vorob'ev, Yu. F. Popov, A. P. Pyatakov, L. N. Bezmaternykh, and E. A. Popova, JETP Lett. **81**, 272 (2005).
[9] A. K. Zvezdin, A. M. Kadomtseva, Yu. F. Popov, G. P. Vorobev, A. P. Pyatakov, V. Yu. Ivanov, A. M. Kuzmenko, A. A. Mukhin, L. N. Bezmaternykh, and I. A. Gudim, JETP **109**, 68 (2009).
[10] A. M. Kadomtseva, Yu. F. Popov, G. P. Vorobev, A. P. Pyatakov, S. S. Krotov, and K. I. Kamilov, Low Temp. Phys. **36**, 511 (2010).
[11] A. K. Zvezdin, G. P. Vorobev, A. M. Kadomtseva, Yu. F. Popov, A. P. Pyatakov, L. N. Bezmaternykh, A. V. Kuvardin, and E. A. Popova, JETP **83**, 509 (2006).
[12] J. C. Joubert, W. B. White, and R. Roy, J. Appl. Cryst. **1**, 318 (1968).
[13] J. A. Campa, C. Cascales, E. Gutierrez-Puebla, M. A. Monge, I. Rasines, and C. Ruiz-Valero, Chem. Mater. **9**, 237 (1997).
[14] Y. Hinatsu, Y. Doi, K. Ito, M. Wakeshima, and A. Alemi, J. Solid State Chem. **172**, 438 (2003).
[15] A. D. Balaev, L. N. Bezmaternykh, I. A. Gudim, V. L. Temerov, S. G. Ovchinnikov, and S. A. Kharlamova, J. Magn. Magn. Mater. **258-259**, 532 (2003).
[16] E. A. Popova, D. V. Volkov, A. N. Vasiliev, A. A. Demidov, N. P. Kolmakova, I. A. Gudim, L. N. Bezmaternykh, N. Tristan, Yu. Skourski, B. Büchner, C. Hess, and R. Klingeler, Phys. Rev. B **75**, 224413 (2007).
[17] A. I. Pankrats, G. A. Petrakovskii, L. N. Bezmaternykh, and O. A. Bayukov, JETP **99**, 766 (2004).
[18] A. I. Pankrats, G. A. Petrakovskii, L. N. Bezmaternykh, and V. L. Temerov, Phys. Solid State **50**, 79 (2008).
[19] H. Mo, C. S. Nelson, L. N. Bezmaternykh, and V. T. Temerov, Phys. Rev. B **78**, 214407 (2008).
[20] C. Ritter, A. Balaev, A. Vorotynov, G. Petrakovskii, D. Velikanov, V. Temerov, and I. Gudim, J. Phys.: Condens. Matter **19**, 196227 (2007).
[21] C. Ritter, A. Vorotynov, A. Pankrats, G. Petrakovskii, V. Temerov, I. Gudim, and R. Szymczak, J. Phys.: Condens. Matter **20**, 365209 (2008).
[22] J. E. Hamann-Borrero, M. Philipp, O. Kataeva, M. v. Zimmermann, J. Geck, R. Klingeler, A. Vasiliev, L. Bezmaternykh, B. Büchner, and C. Hess, Phys. Rev. B **82**, 094411 (2010).
[23] A. I. Popov, D. I. Plokhov, and A. K. Zvezdin, Phys. Rev. B **87**, 024413 (2013).
[24] F. Yen, B. Lorenz, Y. Y. Sun, C. W. Chu, L. N. Bezmaternykh, and A. N. Vasiliev, Phys. Rev. B **73**, 054435 (2006).
[25] U. Adem, L. Wang, D. Fausti, W. Schottenhamel, P. H. M. van Loosdrecht, A. Vasiliev, L. N. Bezmaternykh, B. Büchner, C. Hess, and R. Klingeler, Phys. Rev. B **82**, 064406 (2010).
[26] M. N. Popova, J. Magn. Magn. Mater. **321**, 716 (2009).
[27] S. A. Kharlamova, S. G. Ovchinnikov, A. D. Balaev, M. F. Thomas, I. S. Lyubutin, and A. G. Gavriliuk, JETP **101**, 1098 (2005).
[28] A. M. Kadomtseva, A. K. Zvezdin, A. P. Pyatakov, A. V. Kuvardin, G. P. Vorobev, Yu. F. Popov, and L. N. Bezmaternykh, JETP **105**, 116 (2007).
[29] S. A. Klimin, D. Fausti, A. Meetsma, L. N. Bezmaternykhm, P. H. M. van Loosdrecht, and T. T. M. Palstra, Acta Cryst. **61**, 481 (2005).
[30] I. A. Sergienko, C. Sen, and E. Dagotto, Phys. Rev. Lett. **97**, 227204 (2006).
[31] H. Katsura, N. Nagaosa, and A. V. Balatsky, Phys. Rev. Lett. **95**, 057205 (2005).
[32] I. A. Sergienko and E. Dagotto, Phys. Rev. B **73**, 094434 (2006).
[33] T. Arima, J. Phys. Soc. Jpn. **76**, 073702 (2007).
[34] R. Hornreich and S. Shtrikman, Phys. Rev. **161**, 506 (1967).
[35] T. Nagamiya, K. Yosida, and R. Kubo, Adv. in Phys. **4**, 1 (1955).
[36] G. T. Rado, Phys. Rev. Lett. **23**, 644 (1969).
[37] J. F. Nye, *Physical Properties of Crystals* (Oxford University Press, Oxford, 1957).
[38] M. N. Popova, T. N. Stanislavchuk, B. Z. Malkin, and L. N. Bezmaternykh, J. Phys.: Condens. Matter **24**, 196002 (2012).
[39] J. S. Griffith, Phys. Rev. **132**, 316 (1963).
[40] S. Washimiya, K. Shinagawa, and S. Sugano, Phys. Rev. B **1**, 2976 (1970).
[41] L. N. Bezmaternykh, S. A. Kharlamova, and V. L. Temerov, Crystallogr. Rep. **49**, 855 (2004).
[42] A. B. Roistin, Sov. Phys. Usp. **14**, 766 (1972), and references therein.
[43] W. B. Mims, *The Linear Electric Field Effect in Paramagnetic Resonance* (Clarendon Press, Oxford, 1976).
[44] W. B. Mims, Phys. Rev. **140**, A531 (1965).
[45] E. J. Bijvank, H. W. den Hartog, and J. Andriessen, Phys. Rev. B **16**, 1008 (1977).
[46] K. E. Roelfsema and H. W. den Hartog, Phys. Rev. B **19**, 2440 (1979).
[47] A. Kiel, Phys. Rev. **148**, 247 (1966).
[48] F. I. B. Williams, Proc. Phys. Soc., London **91**, 111 (1967).
[49] H. B. Callen and E. Callen, J. Phys. Chem. Solids **27**, 1271 (1966).